Cerebral biodistribution and real-time particle tracking *in vivo* of ultrabright fluorescent PLGA nano-carriers

Igor Khalin,[1,3*] *Caterina Severi,*[2] *Doriane Heimburger,*[2] *Antonia Wehn*[1,3], *Farida Hellal*[1,3,4], *Andreas Reisch,*[2*] *Andrey S. Klymchenko*[2*], *Nikolaus Plesnila*[1,3*]

1. Institute for Stroke and Dementia Research (ISD), Klinikum der Universität München, Feodor-Lynen-Straße 17, D-81377 Munich, Germany

2. Laboratoire de Bioimagerie et Pathologies, UMR 7021 CNRS, Université de Strasbourg, Faculté de Pharmacie, 74, Route du Rhin, 67401 Illkirch, France

3. Cluster for Systems Neurology (SyNergy), Munich, Germany

4. Institute of Tissue Engineering and Regenerative Medicine (iTERM), Helmholz Zentrum Muenchen, Ingolstaedter Landstrasse 1, 85764 Neuherberg, Germany

*Corresponding authors: igor.khalin@med.uni-muenchen.de; reisch@unistra.fr; andrey.klymchenko@unistra.fr; nikolaus.plesnila@med.uni-muenchen.de

Key words: poly(lactic-co-glycolic acid), nanocarriers, bulky counterion, drug-delivery, targeting, blood-brain barrier, poloxamer 188.

Abstract

Nanoparticles hold great promise as drug carriers for the central nervous system (CNS), however, knowledge about their biodistribution within the CNS remains fragmentary. To overcome this, we used poly(lactic-co-glycolic acid) (PLGA), a biodegradable polymer approved for the use in humans, to prepare nanocarriers and loaded them with bulky fluorophores. Thereby, we increased single particle fluorescence by up to 55-fold as compared to quantum dots. As a consequence, 70 nm PLGA nanocarriers were visualized by intravital real-time 2-photon microscopy, demonstrating that coating with pluronic F-68 (PF-68) significantly increased the circulation time of PLGA nanoparticles in the blood and facilitated their uptake by cerebral endothelial cells in mice. Using a novel *in vivo* imaging protocol we unambiguously distinguished, by confocal microscopy, nanoparticles' fluorescence from tissue auto-fluorescence and demonstrated how PF-68 coated PLGA NPs were taken up into late endothelial lysosomes within 1 hour. In summary, by increasing the brightness of clinically approved PLGA nanocarriers to a level which allowed *in vivo* detection, we were able to demonstrate that PF-68 shifts the uptake of individual particles from macrophages towards endothelial cells. Our novel technological approach significantly improves the ability to evaluate tissue targeting of nanoscale drug-delivery systems in living organisms, thereby remarkably reducing the gap between their development and clinical translation.

1. Introduction

Nanoparticles (NPs) are promising systems for controlled and targeted delivery of drugs. They have the potential to combine specific delivery and reduced side effects with high patient comfort and may thus significantly improve pharmacotherapy. Among these, polymeric NPs are of particular interest due to their high stability and flexibility. For example, poly(lactic-co-glycolic acid) (PLGA)-based injectable medicines have been approved for human use by the United States Food and Drug Administration and by the European Medicine Agency for decades [1]. Additionally, PLGA is considered as a biocompatible and biodegradable polymer with low toxicity [2] since *in vivo* PLGA is hydrolysed into lactic and glycolic acid and is subsequently metabolized by the tricarboxylic acid cycle. Due to these properties, the interest in PLGA-based drug-delivery systems (DDS) grew significantly in recent years. Their market is expected to reach about 930 billion in 2024 [3] and the FDA has launched a dedicated Regulatory Science Program directed to improve bioequivalence of PLGA-based drug products [4].

Because of the blood-brain barrier, it is particularly difficult to target drugs to the brain [5]. Nano-formulations may overcome these difficulties, but despite substantial efforts, the clinical translation of NPs able to specifically deliver pharmacologically active substances to the brain is still very poor [6]. For example, it was demonstrated that poloxamer 188 (Pluronic F-68, PF-68) coated PLGA nanoparticles may improve CNS drug delivery [7, 8] through the low-dense lipoprotein transport system [9, 10], however, the exact mechanism of nanoparticle-mediated uptake of drugs into the brain remains elusive [11].

One of the reasons responsible for this situation is the limited ability to track individual NPs *in vivo* [10]. NPs-based drug carriers are too small to be directly observed by light microscopy. Therefore, the main strategy employed to overcome this issue was to make fluorescent NPs so bright, that their signal became detectable. Several approaches were developed to increase the brightness of polymer based fluorescent nanoparticles, either using conjugated polymers, like in p-dots [12], or by encapsulating large amounts of dyes [13]. In the latter case, however, high dye concentrations caused self-quenching and reduced particle fluorescence. This issue was finally solved by aggregation-induced emission dyes [14] or, as developed by our team, co-loading NPs with bulky hydrophobic counter-ions [15]. The very high brightness of such NPs allowed us to image individual NPs in cultured cells down to the subcellular level [16-18] and to use Förster Resonance Energy Transfer (FRET) for detection of biomolecules at the single molecule level [19-21]. So far, poly(methyl methacrylate) (PMMA)-based NPs were successfully used for this purpose [22], however, since PMMA is not biodegradable, this

approach has a questionable clinical potential. In the current study we therefore aimed to apply high fluorescence technology based on excitation energy transfer (EET) between bulky dyes to NPs with a clinical potential, *i.e.* PLGA NPs, and to investigate the properties of coated and uncoated with PF-68 NPs in suspension, on surfaces and *in vivo*.

To do so, we first optimized the brightness of PF-68 coated PLGA (PF68-PLGA) NPs by varying the type of dyes, dye loading strategy, and particle size. Then we investigated the biodistribution of these optimized PLGA NPs in the mouse brain *in vivo* by intravital 2-photon microscopy (2PM). Subsequently, we correlated the intravital findings with fixed tissue data using high-resolution confocal microscopy (CM) and a novel 3D-reconstruction protocol allowing the unambiguous spatial distinction of fluorescent signal from individual NPs *in vivo*.

2. Results

2.1 Formulation and characterization of nanoparticles

Dye-loaded PLGA NPs were assembled through nanoprecipitation [23, 24]. A solution of the polymer and the dye in a water-miscible solvent (here acetonitrile) was quickly added to a large excess of an aqueous phase, resulting in supersaturation and formation of nanoparticles **(Figure 1A)**. We chose two types of dye systems with similar spectra for encapsulation: the dye salt R18/F5-TPB, known to be very bright, due to counter-ions which prevent aggregation and self- quenching [15, 22] and the bulky perylene dye lumogen red, which combines very high brightness and photostability [25]. Based on previous data, we chose 1 wt% of the dyes with respect to the polymer as optimum loading. The most straightforward approach to increase NPs brightness is to increase their size, since the number of encapsulated dyes increases with the third power of the radius. A tenfold increase in brightness can thus be achieved by a 2.2-fold increase in size. In the case of nanoprecipitation the particle size depends on the concentration of the polymer, but also on the interactions of charges [26]. Here, we used a polymer concentration of 4 $g \cdot L^{-1}$ and a buffer solution containing NaCl to increase particle size [23, 27]. The role of the NaCl is to screen interactions between charges on the polymer, which influences particle formation, and leads to larger particles [17, 27]. The used combination allowed increasing the particle size from about 30 nm under reference conditions (2 $g \cdot L^{-1}$, 20 mM phosphate buffer, pH 7.4, no additional salt) to around 70 nm, while maintaining a low polydispersity index (PDI) < 0.1. Interestingly, R18/F5-TPB led to slightly bigger particles, which could be further tuned by adjusting the salt concentration. Thereby, we were able to

produce PLGA NPs loaded with lumogen red or R18/F5-TPB with diameters of 70 to 80 nm **(Figure 1B)**.

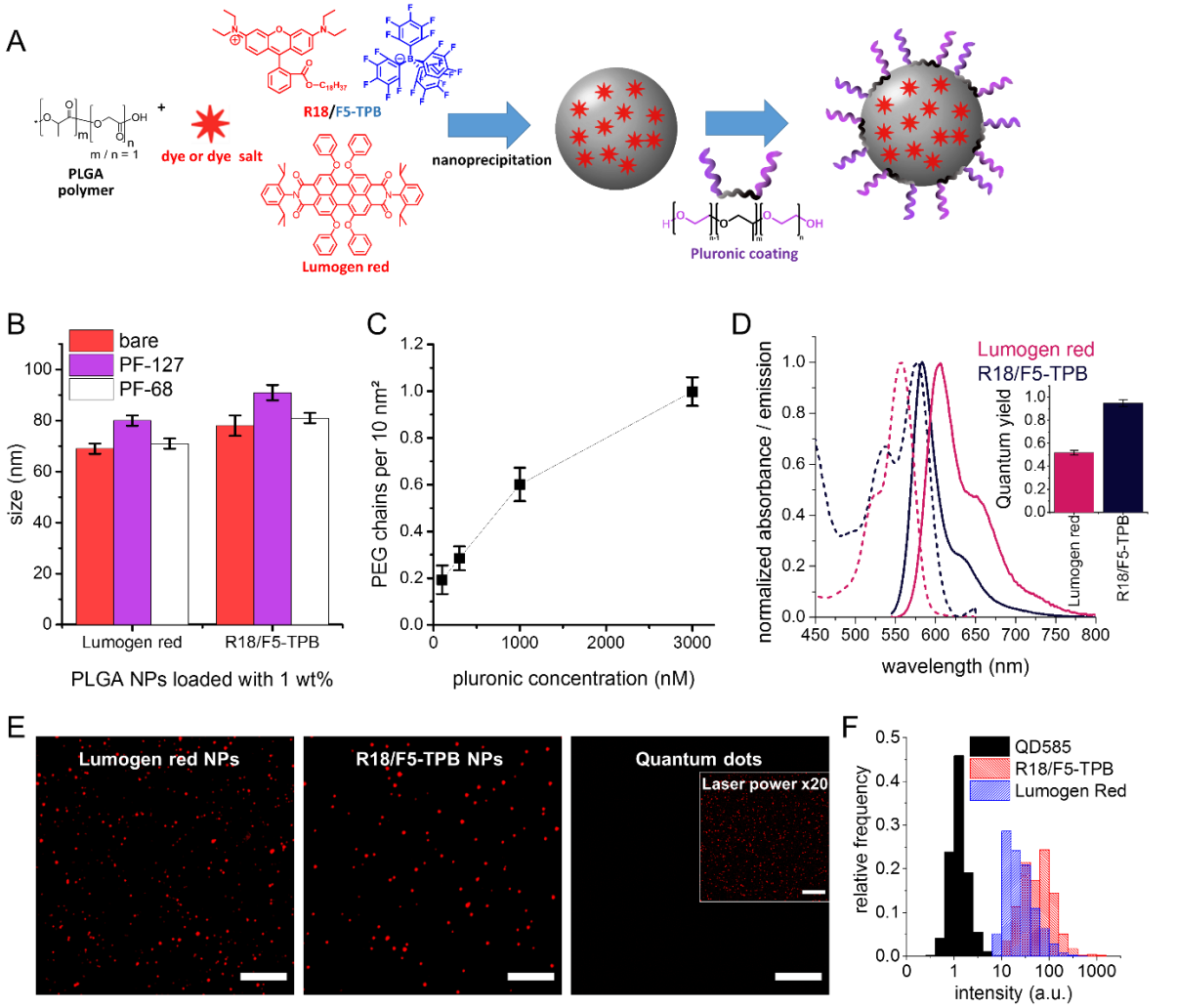

Figure 1. Formulation and analysis of bright PLGA nanoparticles. **A:** Schematic drawing of the assembly of biodegradable dye-loaded PLGA NPs through nanoprecipitation followed by coating with Pluronics. **B:** Sizes of NPs loaded with 1 wt% lumogen red or R18/F5-TPB, either bare or coated with 3000 nM of the Pluronics F-127 or F-68, as obtained by DLS. **C:** Density of PEG chains on the NPs surface at different pluronic concentrations as obtained from FCS measurements using lissamine labelled Pluronic F-127 after dialysis for 24h. Error bars correspond to standard error of the mean for at least three independent measurements. **D:** Normalized absorption (dashed lines) and emission (solid lines) spectra of PLGA NPs. Error bars correspond to three independent measurements. **E:** Fluorescence micrographs of NPs adsorbed on a glass surface. Excitation was 550 nm. To make quantum dots (QDs) visible, the laser power had to be increased by 20 times (insert). Scale bars correspond to 10 µm. **F:** Histograms of particle intensity distribution obtained from based on images from panel (E).

In order to stabilize the particles in biological media and to reduce non-specific interactions, we then adsorbed two types of pluronics, F-127 and F-68, onto the particles. PEGylated particles have been shown to have increased stability in salt and buffer solutions and strongly reduced protein adsorption [17, 26] leading to prolonged circulation half-lives *in vivo* [28]. We

investigated the adsorption of Pluronics with fluorescence correlation spectroscopy (FCS) using Pluronic F-127 (PF-127) labelled with lissamine. This allowed us to directly measure the number of adsorbed pluronics per single NP (here NPs of 30 nm were used in order to avoid perturbations of the FCS measurements) depending on the added concentration **(Figure 1C)**. The density of pluronics and, in consequence, the density of PEG chains on the surface of NPs increased continuously up to a concentration of 3000 nM. At this concentration about 100 pluronics per NP remained on the surface after dialysis. This corresponds to about one PEG chain per 10 nm², a value well in line with previous results [28, 29]. Adsorption of pluronic PF-127 or PF-68 onto the surface of NPs increased the particle size by 10 and 4 nm, respectively **(Figure 1B)**. This increase in size indicates the formation of a PEG shell around the NPs.

Encapsulation of the dyes within NPs resulted in absorption and emission spectra similar to those of the dyes in solution, indicating minimal aggregation of the dyes within NPs **(Figure 1D, Figure S1)**. The quantum yields (QY) of R18/F5-TPB and lumogen red remained at a very high level (95 and 52%, respectively) as determined from the absorbance and fluorescence spectra, using Rhodamine 101 as reference[30]. Based on the particle size and loading, it can be estimated that particles contained about 1000 dyes in the case of lumogen red and 1150 in the case of R18/F5-TPB. Using the absorption coefficients of the dyes ($\varepsilon \approx 100{,}000\ M^{-1}.cm^{-1}$ for R18/F5-TPB and $\approx 75{,}000\ M^{-1}.cm^{-1}$ for lumogen red) the particle brightness can be estimated by $N \times \varepsilon \times QY$, where N is the number of dyes per particle: $1.1 \times 10^{8}\ M^{-1}.cm^{-1}$ for the R18/F5-TPB NPs and $4.0 \times 10^{7}\ M^{-1}.cm^{-1}$ for the lumogen red NPs. This brightness can be compared to that of quantum dots of similar color (here QD585 from Invitrogen), a common, commercially available standard for bright NPs. At an excitation wavelength of 550 nm (using our microscopy setup) the QD585 brightness was about $\sim 2.1 \times 10^{5}\ M^{-1}cm^{-1}$ (estimated form the data of provider), *i.e.* at least two orders of magnitude higher than QDs. It should be noted that QD585 exhibit a ~10-fold higher absorbance (and thus higher brightness) in the violet spectrum (405 nm), but for a direct comparison with our NPs, we used the identical conditions. We further compared single-particle brightness by wide-field fluorescence microscopy, after deposition of the particles on glass surfaces at dilutions maximizing the deposition of individual particles [15]. This comparison revealed that lumogen red and R18/F5-TPB NPs have a 23 and 55 times higher brightness than quantum dots, respectively **(Figure 1E,F)**. The lower values obtained here are due to a combination of multiple factors. First one is an overestimation of the particle size (and thus the number of dyes per particle) by DLS, which provides hydrodynamic diameter rather than the size [21] of the particle core. Second, relatively strong irradiation power used under

the microscope, compared to the fluorometer, may lead to saturation behavior in the multi-chromophore system due to phenomena of singlet-singlet annihilation [31].

2.2 Intravital evaluation of systemic circulation of PLGA NPs

Our next step was to investigate whether lumogen red loaded PLGA NPs coated with PF-68 can be visualized *in vivo*. We implanted an acute cranial glass window over the cerebral cortex of a mouse, inserted a femoral arterial catheter for systemic injection of NPs, and placed the animals under a 2-photon microscope as previously described [28]. Such a system allowed us to inject the NPs solution into the mouse while it was placed under microscope. After visualizing cerebral vessels with a plasma tracer (fluorescein isothiocyanate (FITC)-dextran 2000 kDa; **Figure 2A; Baseline**), we chose a region of interest (ROI) and injected PLGA NPs

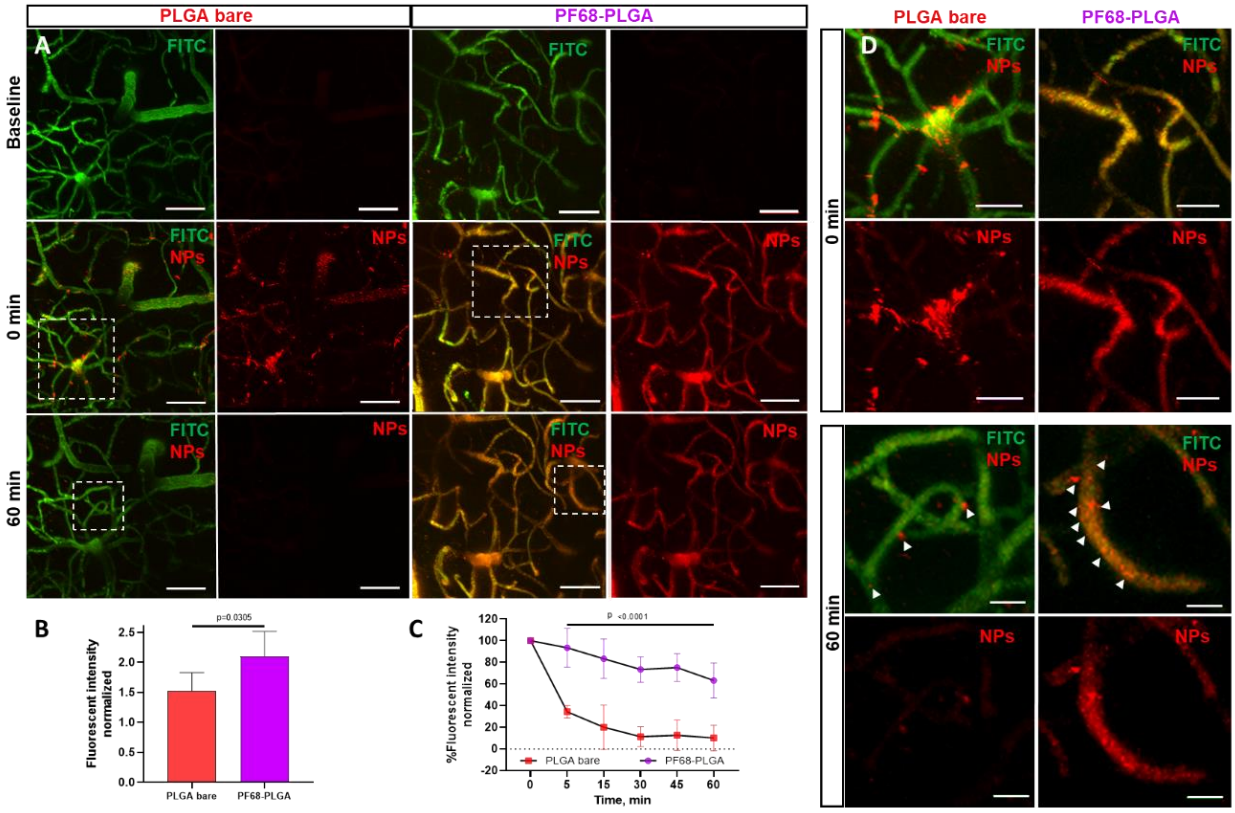

Figure 2. Intravital 2-photon microscopy of PLGA NPs in mouse brain vasculature. **A:** 2-photon microscopy (2PM) images after injection of FITC-dextran 2000kDa to label blood plasma (Baseline) and immediately (0 min) or 60 minutes after additional injection of bare or PF-68 coated PLGA (PF68-PLGA) NPs. Scale bars: 20 μm. **B:** Quantification of fluorescence intensity of circulating coated and not coated PLGA NPs immediately after injection. **C:** Temporal kinetics of the fluorescence intensity of bare vs. PF68-PLGA NPs quantified from 2-PM images. Data presented as means ± standard deviation. Statistical analysis: two-way ANOVA with Tukey correction for multiple comparison (bare NPs n=3, coated NPs n=6). **D:** High power images of the regions indicated by the dotted squares in A. White arrows: NPs stuck in the vessel wall. Scale bars: 10 μm.

loaded with lumogen red with and without PF-68 coating. In both groups we immediately observed circulating PLGA NPs in the brain vasculature **(Figure 2A; 0 min)**. Sixty minutes after injection, bare NPs were almost undetectable, while coated NPs were clearly visible **(Figure 2A; 60 min)**. Despite the fact that bare and coated NPs were injected at equal doses (7.5 $\mu L \cdot g^{-1}$), the absolute fluorescence intensity of coated NPs was significantly higher than the one of bare NPs right after injection **(Figure 2B)**. Quantification of relative intravascular fluorescence intensities over time showed that the intensity of bare NPs dropped steeply to 35% of baseline already 5 minutes after injection and became negligible 25 minutes later. In contrast, 63% of the initial fluorescence intensity of PF68-PLGA NPs was still present even one hour after injection **(Figure 2C)**. These *in vivo* data demonstrate that lumogen red-loaded PLGA NPs coated with PF-68 are sufficiently bright and have a half-life for more than 1 h.

To better understand why bare NPs have a reduced fluorescence intensity right after injection and how PEG-shell stabilizes the NPs in the blood, we analysed zoomed areas marked by dotted squares in figure 2A at higher magnification. Bare PLGA NPs (PLGA bare) presented as dispersed heterogeneous aggregates with varying fluorescence intensities; some aggregates seemed to stick to circulating blood cells **(Figure 2D, left; 0 min and Movie S1)**. In contrast, PF68-PLGA NPs produced a homogenous fluorescence signal within the vascular lumen and circulated without any obvious stalls early after injection **(Figure 2D, right; 0 min and Movie S2)**. Due to the high velocity of cerebral blood flow and the low maximal frequency of the 2-PM scanner, coated particles could not be detected individually. One hour after injection, practically no bare NPs could be observed **(Figure 2D, left; 60 min)**, while coated PLGA NPs were still present within the vessel lumen and emitted a bright fluorescence **(Figure 2D, left; 60 min)**. Interestingly, we detected that few uncoated and a large number of coated PLGA NPs did not circulate, but became associated with the vessel wall, suggesting adhesion to the endothelial surface or endothelial uptake **(Figure 2D, 60 min, white arrows)**. We followed the NPs for another 60 min, *i.e.* until 120 minutes after injection, but did not observe major changes **(Figure S2)**; PLGA NPs were still aligned with the vessel wall.

2.3 Analysis of the PF-68 PLGA NPs bio-distribution in post-fixed brain

To exclude any influence of craniotomy and since 2-PM intravital imaging does not have the necessary resolution to distinguish between adhesion of NP to the vessel wall and uptake of NPs by endothelial cells, we continued our investigations using perfusion-fixed brain tissue and high-resolution confocal microscopy. For this purpose, naïve mice, i.e. mice without a cranial window, were sacrificed 60 minutes after intravenous injection of PBS (control), bare, or coated PLGA NPs and histological sections from brain, heart, spleen, liver, and kidney were evaluated

for particle fluorescence by observational confocal microscopy **(Figure S3A)**. Tissue from animals which received PBS showed a red background fluorescence without any fluorescent signal indicative of NPs **(Figure S3B, top row)**. In contrast, the tissues from animals which received bare **(Figure S3B, middle row)** or coated PLGA NPs **(Figure S3B, bottom row)** showed a significant increase in the red fluorescence. Quantification of fluorescence intensity demonstrates that the strongest signal by far was detected in the liver followed by the spleen, the kidney, the heart, and the brain **(Figure S3C)**. Since animals were perfused before the organs were removed, these findings indicate that one hour after injection most PLGA NPs were mainly taken up by the liver and the spleen, organs well known for the phagocytic activity, but accumulated also other organs, including the brain. To identify which cells within the brain took up the PLGA NPs, we scanned brain coronal sections with high magnification confocal microscopy using 40 and 100x objectives (**Figure 3A,B**).

In whole brain tiles and plane scans (**Figure 3A,B**) we detected that the red fluorescent signal was more intense in animals which received PLGA NPs. Moreover, the intensity in the brain was 2-fold higher for coated NPs compared with PBS (**Figure 3C**), while it did not exceed 20% at 25x magnification **(Figure S3 C)**. However, spatial NPs distribution was still not possible to define. Therefore, we decided to increase the magnification up to 100x. Surprisingly, images taken at even higher magnification (100x) showed discrete red fluorescent foci not only in tissue from mice which received PLGA NPs, but also in control animals (**Figure 3D**, **i**). When switching to the green channel (**Figure 3D**, **ii**), it became apparent that some of the fluorescent foci in the red channel also emitted green fluorescence indicating auto-fluorescence, *i.e.* fluorescence not generated by NPs, but by other structures in the brain, *e.g.* lipofuscin. In fact, most of the auto-fluorescent signals were located around the nuclear structures. When merging the red and the autofluorescence (green) channels (**Figure 3D**, **iii**), all fluorescent signals observed in brain tissue from control mice turned out to be colocalized, thus caused by auto-fluorescence (**Figure 3D**, **iii, yellow arrows**), while in animals which received PLGA NPs also red, (non-colocalized) foci without a corresponding signal in the green channel were observed (**Figure 3D**, **iii, white arrows**). As such, we excluded non-specific auto-fluorescence and retrieved the true NPs fluorescence. Using this approach, we were able to unambiguously identify individual PLGA NPs in brain tissue. Important to keep in mind that spot sizes in the optical microscopy images depend on the microscope settings and the particle brightness and are in the end limited by diffraction (typical resolution at this wavelength ~300 nm). There is as such no direct relation between particle size and spot size in the microscope image.

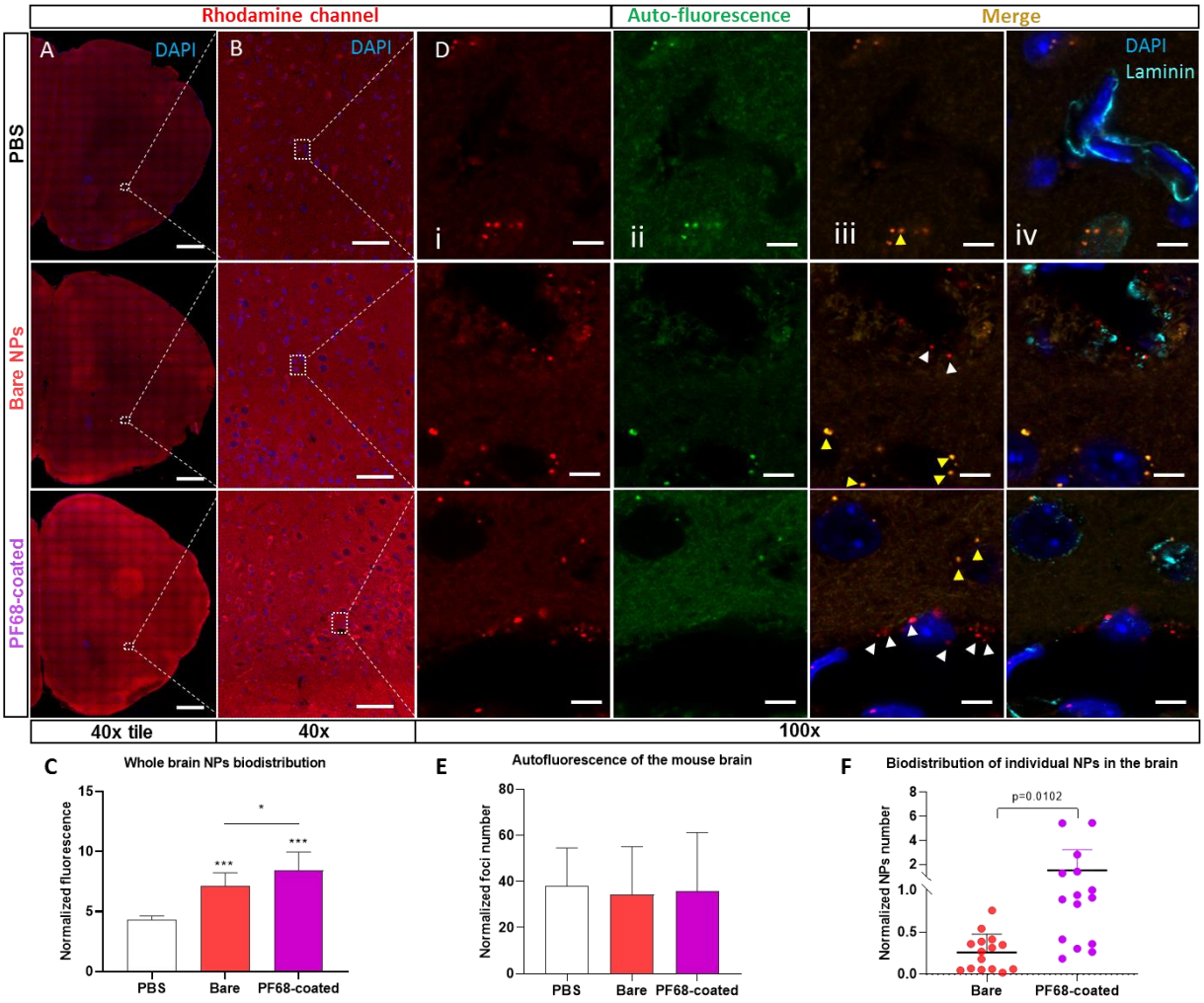

Figure 3. Biodistribution of F68-coated NPs in the mouse brain 60 minutes after systemic application. Confocal microscopy images of coronal brain section recorded with an 40x objective from mice which received PBS, bare, or coated red fluorescent PLGA NPs. **A:** Tile scan of whole section and **B:** a single scan. Nuclei were stained with DAPI. Scale bars: 1mm (40x tile), 50 µm (40x single). **C:** Quantification of the distribution of the NPs throughout the whole brain, analysed using FIJI: the mean grey value of the rhodamine channel normalized to the mean grey value of the DAPI channel. Data presented as means ± standard deviation (SD). For the statistical analysis, one-way ANOVA was used followed by multiple comparison with the Tukey correction. *** $p<0.001$ compared to PBS group; * $p<0.05$ compared to F68-coated group; (n=3 animals x 3 whole brain regions (rostral, middle, caudal)). **D:** A zoomed single plane from **B** of brain parenchyma, stained by Laminin and DAPI. **i:** Rhodamine channel shows non-specific red foci. **ii:** Auto-fluorescent channel shows auto-fluorescent foci of the brain parenchyma. **iii**: Merge channels show true NPs signal which appeared only in rhodamine channel. White arrows indicate the PLGA NPs, while yellow arrows indicate auto-fluorescence as a co-localization between rhodamine and auto-fluorescent channels. **iv:** Basal lamina stained by Laminin outlines the spatial distribution of NPs. Scale bar - 5 µm. **E:** Quantification of the autofluorescent foci (co-localized with autofluorescent channel) and **F:** PLGA NPs distribution (non-colocalized with autofluorescent channel). Foci or PLGA NPs found in the region of interest (ROI) was normalized to the ROI area (μm^2) and cell numbers (n=3 x ROI=5). Data presented as mean ± SD. For the statistical analysis of autofluorescence, one-way ANOVA was used followed by multiple comparison with the Tukey correction; for the NPs - unpaired t-test.

To further unravel the cellular distribution of PLGA coated NPs in the brain, we stained the basal lamina with anti-laminin antibodies (**Figure 3D**, **iv)**. After 3D-reconstruction, we observed that bare and coated PLGA NPs were located inside the luminal part of the basement membrane **(Movie S3)**, suggesting that NPs were not able to cross the BBB, but were

internalized by endothelial cells. Taken together, using high-resolution confocal microscopy, correction for unspecific auto-fluorescence, and 3D-reconstructions, we demonstrate that PF68-PLGA NPs accumulate within the brain by being entrapped in endothelial cells.

Furthermore, quantitative analysis of the brain sections described above, demonstrated that mice, which received red fluorescent PLGA NPs, emitted significantly more fluorescence than control brain tissue (**Figure 3C**), suggesting accumulation of NPs in the brain. In addition, quantification of auto-fluorescence in the same tissue sections, showed that, as expected, all experimental groups emitted the same amount of auto-fluorescence, *i.e.* fluorescence not deriving from NPs (**Figure 3E**). When correcting the total particle count for the auto-fluorescence signal, it became apparent that PF68-coated NPs accumulated at 8-times higher numbers than uncoated NPs (**Figure 3F**). As such, this method could improve the signal-to-noise ration from 20% **(Figure S3 C)** to 800% (**Figure 3F**) and clearly detect that coating with PF-68 may facilitate the accumulation of NPs within the brain. However, we do not know whether by an enhanced specific interaction of coated NPs with the endothelial cell membrane, like commonly suggested [9-11], or merely by an increased contact time with the vessel wall due to a longer plasma half-life **(Figure 2C)**.

In order to investigate the bio-distribution of coated NPs at the subcellular level, we stained late lysosomes, the cellular structures suspected to be involved in the uptake of NPs from the extracellular space, using the specific marker lysosomal-associated membrane protein 1 (LAMP-1; **Figure 4A)**. Using the same technique, to avoid unspecific signals **(Figure 4B, i)** as described above, *i.e.* adding auto-fluorescence signals to the particle-specific rhodamine channel, we were able to clearly distinguish between yellow auto-fluorescent structures **(Figure 4B, ii, yellow arrow)** and red NP-specific signals within capillary endothelial cells **(Figure 4B, ii, red arrows)**. When colocalising NP-specific signals with LAMP-1, we identified NPs located in lysosomes **(Figure 4A, iii, magenta arrows)**. To confirm this colocalization, we took advantage of the depth information obtained by confocal microscopy and performed 3D-reconstructions of the area of particle accumulation (**Figure 4C, Movie S4**). Indeed, we found a large number of empty lysosomes (**Figure 4C, white spheres**) and lysosomes emitting autofluorescence (**Figure 4C, red/green spheres, yellow arrow**), however, next to free NPs (**Figure 4C, red spheres, red arrows**), we also found NPs co-localizing with the LAMP-1 signal (**Figure 4C, red/white spheres, magenta arrows**). Altogether, these findings clearly suggest, that PLGA NPs were taken by brain endothelial cells and ended up in late lysosomes. Previously, addressing such questions was possible only by means of electron microscopy.

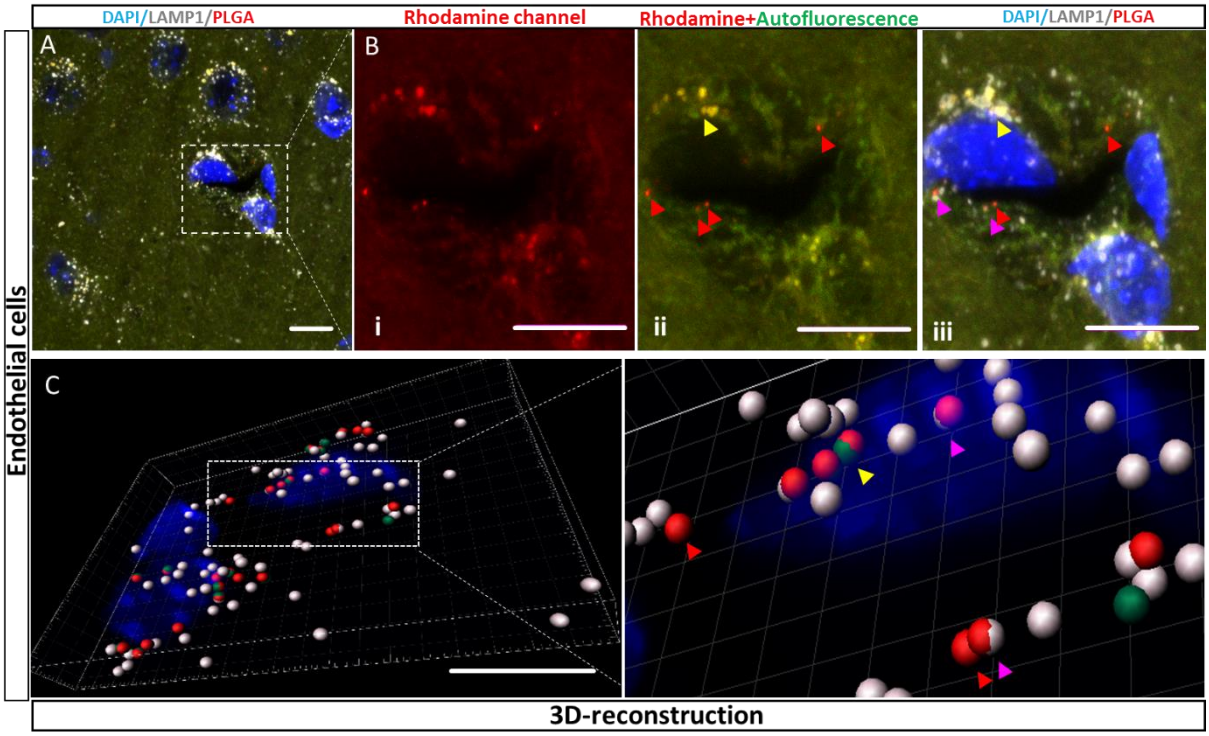

Figure 4. Intracellular distribution of coated PLGA NPs in brain capillary endothelial cells. A: A brain capillary identified by its lumen and three nuclei (blue) of vessel wall cells. Vascular cells contain a number of lysosomes as identified by LAMP-1 antibodies (white). **B**: Rhodamine channel. The vessel wall emits a large number of red particle-like fluorescence signals. **ii**: Green auto-fluorescence channel merged with rhodamine channel. Auto-fluorescence (yellow arrow) and red fluorescence emitted by NPs (red arrow). **iii:** LAPM-1 signal suggests that next to free NPs (red arrows), some NPs are taken up into lysosomes (magenta arrows). **C:** 3D reconstruction of the image shown in **A.** White spheres indicate LAMP1 positive cell compartments, red spheres NPs, and green spheres auto-fluorescent structures. Most lysosomes are empty, however, next to lysosomes emitting auto-fluorescence (red-green spheres, yellow arrow) a number of lysosomal signals also colocalise with NPs fluorescence (red-white spheres, magenta arrows). Scale bars: 5 µm.

Then, we explored whether uptake of NPs by endothelial cells was a brain specific event or if it also occurred in other tissues. For this purpose, we stained liver, spleen, kidney, and heart with collagen IV, a specific marker of the vascular basement membrane [32] **(Figure 5A)**. We found significant uptake of both bare and coated PLGA NPs in these internal organs **(Figure 5A)**. By quantitative analysis using the Manders colocalization coefficient [33] **(Figure 5A,B)**, we have identified that level of colocalization of coated NPs with vessels was significantly higher compared to bare in all discovered internal organs **(Figure 5B)**, meaning that coating is promoting the endothelial uptake of NPs in internal organs. Hence, coating promotes NPs to accumulate not only in the brain, but also in peripheral endothelial cells.

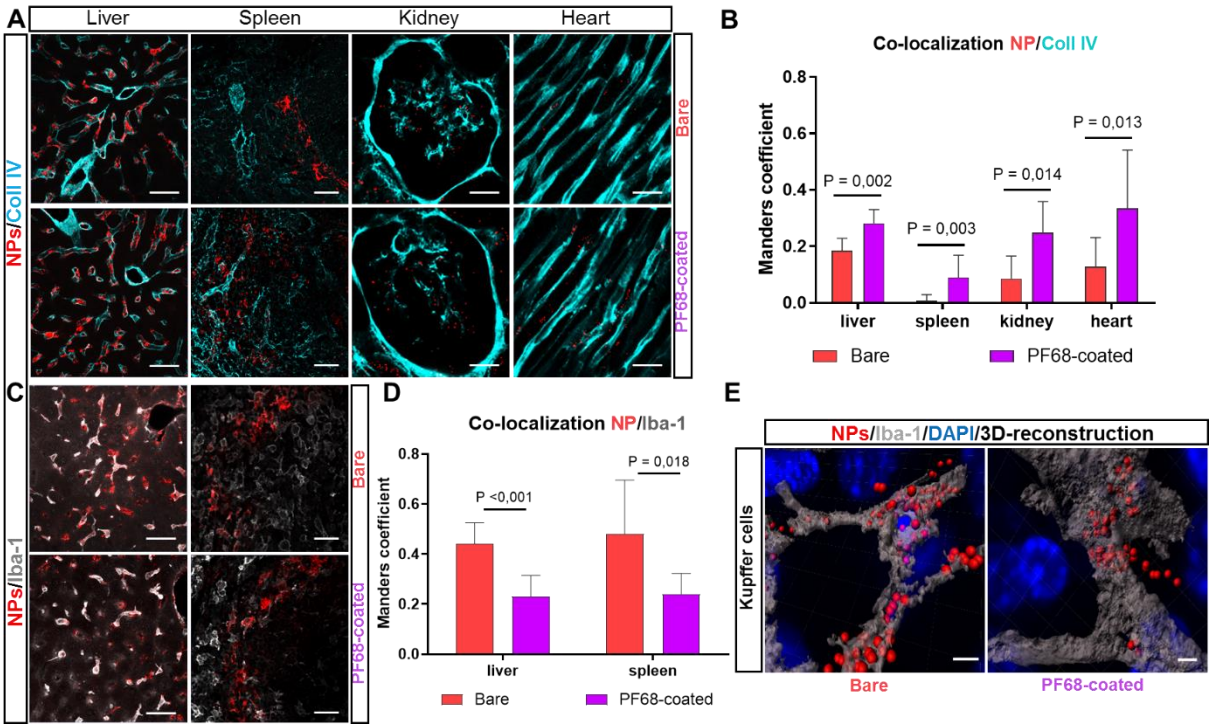

Figure 5. Uptake of PLGA NPs by endothelial and immune cells of the liver, spleen, kidney and heart. Representative confocal images of collagen IV **(A)** and Iba-1 **(C)** stained sections of from animals injected with bare and coated NPs. Maximum intensity projection of merged rhodamine and 647 nm channels. Scale bar: 20 µm. Quantification of co-localization of bare and coated NPs with collagen IV **(B)** and Iba-1 **(D)** using the FIJI JACoP Plugin. For the statistical analysis, Mann-Whitney Rank Sum Test was used; n=3 mice and 3-4 ROIs per section. **E:** Representative 3D reconstruction of 100x confocal images of Kupffer cells containing bare (left) and coated (right) NPs. Blue – DAPI, red spheres – PLGA NPs, grey surface – Kupffer cell. Scale bar: 3 µm.

Finally, we investigated colocalization of NPs with ionized calcium-binding adapter molecule 1 (Iba-1), a specific marker for phagocytic cells [34], *i.e.* Kupffer cells in the liver and red pulp macrophages in the spleen. We observed significant colocalization of bare and coated NPs fluorescence with iba-1 phagocytic cells in liver and spleen tissue. Interestingly, bare NPs were more readily taken up by macrophages than coated ones **(Figure 5C,D)**. To evaluate this finding on a cellular and subcellular level, we performed 3D reconstructions of individual Kupffer cells. This high-resolution approach unambiguously demonstrated a higher number of bare PLGA NPs inside the cytoplasm of Kupffer cells; the uptake of PF-68 coated NP was much less efficient **(Figure 5E, Movie S5, S6)**, suggesting that PF-68 coating decreased phagocytosis of NPs on the level of each individual macrophage.

Taken together, our results demonstrate that bare PLGA NPs are readily taken up by phagocytic cells in liver and spleen. Coating with PF-68 increases endothelial uptake and reduces phagocytosis by macrophages significantly. These data suggest, that PF-68 coating

systemically shifts the uptake of PLGA NPs from phagocytic cells towards endothelial cells. In the brain *in vivo* real time imaging by 2-photon microscopy and high resolution immunohistochemistry demonstrate that NPs are compartmentalized in late lysosomes and neither bare nor coated PLGA NPs reach the brain parenchyma. Thus, PF-68 coating of PLGA-NP increases endocytosis of NPs by endothelial cells.

3. Discussion

We strikingly increase the fluorescent intensity of PLGA NPs by loading bulky fluorescent dyes: lumogen red or rhodamine B derivative with bulky counter-ions. Thereby, we obtained biocompatible and biodegradable NPs with a fluorescence 23-55 times higher than quantum dots (QD585 at 550 nm excitation), the current golden standard, and were able to directly visualize their spatial-temporal biodistribution *in vivo* by 2-photon and confocal microscopy. Using this approach, we demonstrate that, within 1 hour, PLGA NPs are readily taken up by macrophages in liver and spleen and that coating with PF-68 significantly shifts their uptake towards endothelial cells. In cerebro-vascular endothelial cells PF68-coated PLGA NPs are compartmentalized in lysosomes, *i.e.* NPs do not enter the brain parenchyma. To our knowledge, this is the first report describing the biodistribution of individual PLGA NPs, an FDA-approved drug delivery system (DDS), dynamically and with subcellular resolution *in vivo*.

The current development of highly fluorescent PLGA NPs was based on a previous study using EET with counterion strategy [28], where we demonstrated *in vivo* tracking of PMMA-SO_3 NPs. However, here we made a step towards clinical translation by changing the polymer to biocompatible and biodegradable (PLGA). It brought some unexpected issues: having the same size of ~74 nm, PMMA-SO_3 NPs could be resolved as single units in the blood stream of mice even when imagined in cerebral vessels which are known for their high blood flow velocity, while PLGA NPs could only be detected as individual particles when immobilized at or within the vessel wall. We assume that in the less hydrophobic PLGA dyes may tend to cluster, while in the more hydrophobic PMMA NPs dyes may disperse more homogenously, leading to a higher QY and higher per particle brightness for PMMA NPs [22]. Additionally, the pharmacokinetics of same size NPs from both studies was not identical, demonstrating that NPs made of other polymers may not be used as proxies for the whole class of NPs, since significant differences may exist even in the way how NPs take up labelling molecules, i.e. each individual NP formulation needs to be tested separately, ideally *in vivo*.

When evaluating the pharmacokinetics of fluorescently labelled NPs *in vivo*, false positive results are a common issue due to leaking of fluorophores from NPs and unspecific binding to other structures. For example, up to 28-68% of Rhodamine B or ATTO488 fluorescence was shown to dissociate from liposomes in human plasma [35]. In our study, we solved this problem by using very hydrophobic counterions to increase the hydrophobicity of the resulting dye salt and in this way improved encapsulation and strongly reduced leaking [36]. Moreover, high hydrophobicity of limogen red also prevented leakage from PLGA in NPs, in line with previous data in serum and cells [25]. On the other hand, we kept in mind that EET-related high brightness of the NPs [15], does not occur when dye molecule leaks, thus fluorescence decreasing to very low levels and becoming undetectable. Therefore, false positive labelling due to leaked dyes was not an issue in the current study.

A major challenge of the specific detection of NPs in the fixed brain is the strong auto-fluorescence of cerebral tissue after PFA exposure deriving, among others, from, mitochondria, collagen, or lipofuscin [37]. Currently used autofluorescent quenching kits [38] are able to solve this problem just partially by removing only non-lipofuscin sources. Cerebral autofluorescence, however, is highly abundant in lipofuscin and is often particularly strong in structures of the same size and brightness as NPs. Therefore, broad emission spectrum cerebral auto-fluorescence often generates signals which very closely mimic NPs and may also generate false positive results. In the current study, we detected strong autofluorescent deposits in neurons and endothelial cells, findings well in line with the literature [39]. Subsequently, we avoided false positive identification of NPs by additional scanning of a channel outside the emission rage of NP fluorescence. Signals detected in this channel were regarded as autofluorescence and used to correct NP counts for false positive events. Since such an approach is rarely used when evaluating the biodistribution of NPs by histology, we would recommend this approach for all future analysis of DDS biodistribution in the CNS.

Using autofluorescence correction, we quantified the uptake of PLGA NPs by brain tissue with high resolution and specificity and demonstrated increased uptake after PF-68 coating. Moreover, we clearly showed that particles do not pass beyond the capillary basement membrane, *i.e.* do not cross the BBB. Our findings suggest, that mechanism of NPs brain uptake is associated with endocytosis by endothelial cells and that NPs consequently end up in late lysosomal vesicles without further passage into the brain. Our findings are important for any future studies in LDL-related endothelial receptor-mediated transcytosis as well as for a plethora of completed studies which reported that PF-68 coating enhances the CNS action of pharmacologically active cargo molecules [9, 11]. Despite the mechanism of interaction with

the surface of endothelial cells is known to be associated with the LDL-receptors [9], in fact, none of these studies univocally demonstrated *in vivo* that used NPs crossed the BBB. One explanation to resolve this discrepancy is that NP trapped in late lysosomes release their cargo which then diffuses into the brain parenchyma. The other is that we overlooked NPs which have already been dissolved and delivered their cargo, because, we detected only intact particles. Further experiments using the currently developed *in vivo* tracking technology enhanced by techniques able to detect cargo delivery on the cellular and subcellular level may resolve this important issue in the future.

Coating of NPs with poloxamer 188 was reported to reduce phagocytosis by liver and spleen macrophages [40] and we could reproduce these results with this coating, though to a lower extent. More importantly, however, we demonstrated by *in vivo* confocal imaging at single-particle resolution that coating of NPs with PF-68 shifted the uptake of NPs from immune towards endothelial cells. This observation was not only present in the brain, but also in all other investigated organs, *i.e.* liver, spleen, kidney, and heart; and whether it happened due to longer circulation of the NPs or specific transport would be a question for further research. All in all, identifying such a shift from one to another cellular compartment *in vivo* with high fidelity convincingly demonstrates the potential of the currently developed experimental approach for the specific detection of NPs in a living organism.

4. Conclusions

Taken together, we developed novel, highly fluorescent biocompatible and biodegradable PLGA NPs and demonstrate the bio-distribution of these FDA approved drug delivery systems in the mouse *in vivo* at single particle resolution by single- and multi-photon microscopy. Using this novel experimental approach, we demonstrate that uncoated PLGA NPs are mainly taken up by liver and spleen macrophages, while PF-68 coating shifts the uptake towards endothelial cells. In the brain, PF68-coated PLGA NPs end up in late endothelial lysosomes. Thus, the combination of novel, highly fluorescent PLGA NP with high resolution *in vivo* imaging, and strategies to avoid unspecific autofluorescence allowed us to unambiguously detect the biodistribution of NPs down to the subcellular level with so far unprecedented accuracy, specificity, and resolution. This may help to significantly close the existing translational gap between the preclinical and clinical evaluation of NPs.

5. Material and methods

5.1 Materials. Poly(D,L-lactide-co-glycolide) (PLGA, acid terminated, lactide:glycolide 50:50, M_w = 24,000-38,000), poloxamer 407 (Pluronic F-127) and poloxamer 188 (Pluronic F-

68), propargylamine (98%), copper(II) sulfate pentahydrate (98.0%), sodium ascorbate (>98.0%), sodium azide (99%), sodium chloride (molecular biology grade), triethylamine (TEA, >99.5%), acetonitrile (anhydrous, 99.8%), dichloromethane (anhydrous, >99.8%), and N,N-dimethylformamide (absolute >99.8%) were purchased from Sigma-Aldrich. N,N-diisopropylethylamine (DIPEA, >99.0%), methanesulfonyl chloride (>99.7%), and 2-aminoethane sulfonic acid (taurine, >98.0%) were obtained from TCI. 1-hydroxybenzotriazole (HOBt, >99.0%), N-tetramethyl-O-(1H-benzotriazol-1-yl)uronium hexafluorophosphate (HBTU, 99.5%), and 1-[bis(dimethylamino)methylene]-1H-1,2,3-triazolo[4,5-b]pyridinium 3-oxid hexafluorophosphate (HATU, 99.8%) were purchased from chemPrep. Sodium phosphate monobasic (>99.0%, Sigma-Aldrich) and sodium phosphate dibasic dihydrate (>99.0%, Sigma-Aldrich) were used to prepare 20 mM phosphate buffer solutions at pH 7.4. MilliQ water was deionized using a Millipore purification system. R18/F5-TPB was synthesized from rhodamine B octadecyl ester perchlorate (Aldrich, >98.0%) and lithium tetrakis(pentafluorophenyl)borate ethyl etherate (AlfaAesar, 97%) through ion exchange followed by purification through column chromatography as described previously [15, 41]. N,N-Bis-(2,6-diisopropylphenyl)-1,6,7,12-tetraphenoxy-3,4,9,10-perylenebis(dicarboximide) (Lumogen Red) was purchased from ORGANICA® Feinchemie GmbH Wolfen.

5.1.1 Sulfonated lissamine-alkyne was synthesized as described previously [28, 42]. Briefly, lissamine, (100 mg, 0.16 mmol, 1 eq), propargylamine (11 mg, 0.19 mmol, 1.2 eq), HATU (76 mg, 0.16 mmol, 1 eq), and DIPEA (127 µL, 0.75 mmol, 5 eq) were solubilized in anhydrous DMF (5 mL) under argon. After stirring at room temperature for 24h, the mixture was dried under reduced pressure at 65°C and then diluted with DCM (20 mL) and extracted four times with water. The combined organic phases were dried over sodium sulfate and concentrated *in vacuo* and, subsequently, the residue was purified by flash chromatography eluting with DCM/MeOH (99:1) to give 89.5 mg of a pink solid (yield: 54%).

^{1}H NMR (400 MHz, MeOD): δ = 8.65 (1H, s, ar. CH) + 8.03 (1H, d, ar. CH) + 7.29 (1H, d, ar. CH) + 7.16 (2H, d, ar. CH) + 6.85 (2H, d, ar. CH) + 6.73 (2H, s, ar. CH) ~9H, 3.95 (2H, s, -NCH_2C-), 3.51-3.65 (8H, m, -NC*H_2*CH_3), 2.45 (2H, t, -NCOCH_2-), 2.27 (1H, s, CCH), 1.23-1.34 (12H, m, -NCH_2C*H_3*).

5.1.2 Dimesyl derivative of PF-127. PF-127 (6.3 g, 0.5 mmol, 1 eq) was solubilized in DCM (25 mL) and cooled to 0°C. Next, TEA (420 µL, 3 mmol, 6 eq), and methanesulfonyl chloride (234 µL, 3 mmol, 6 eq) were added. The reaction mixture was kept under stirring at 0°C for 3 h and then at room temperature overnight. The solution was dried under reduced pressure at 40°C for 30 minutes. The obtained solid was redispersed in water and purification

is carried out by means of dialysis against water (48 h) to give 5.2 g of a white solid (yield: 82%).

^{1}H NMR (400 MHz, MeOD): δ = 3.81-3.78 (4H, m, -SOCH$_2$*CH$_2$*-), 3.77-3.61 (-O*CH$_2$CH$_2$*O-) + 3.59-3.51 (m, -O*CH$_2$*CH-) + 3.43-3.38 (m, -*CH*CH$_3$) ~1000H, 3.14 (6H, s, C*H$_3$*SOO$^-$), 1.16 (~195H, m, -CH*CH$_3$*).

5.1.3 Diazide derivative of PF-127. The dimesyl derivative of PF-127 (5.2 g, 0.41 mmol, 1 eq) and sodium azide (165 mg, 2.46 mmol, 6 eq) were solubilized in acetonitrile (25 mL) and heated under reflux for 48 h. The obtained solid was redispersed in water and purification was carried out by means of dialysis against water (48h) to give 4.6 g of a white solid (yield: 87%).

^{1}H NMR (400 MHz, MeOD): δ = 3.77-3.61 (-O*CH$_2$CH$_2$*O-) + 3.59-3.51 (m, -O*CH$_2$*CH-) + 3.43-3.38 (m, -*CH*CH$_3$ + *CH$_2$*N$_3$) ~1000H, 1.16 (~195H, m, -CH*CH$_3$*).

5.2 Click reaction of lissamine on pluronic. Sodium ascorbate (13 mg, 0.074 mmol, 16.5 eq in 100 µL of water) was added to a Copper(II) sulfate pentahydrate (10 mg, 0.04 mmol, 9 eq in 100 µL of water). Then the solution was added in a mixture of diazide derivative of PF-127 (55 mg, 0.0045 mmol, 1 eq), and sulfonated lissamine-alkyne (9 mg, 0.013 mmol, 2.9 eq) dissolved in anhydrous DMF (5 mL). The heterogeneous mixture was stirred vigorously for 24 hours at 55°C under argon. The reaction mixture was dried under reduced pressure at 60°C, diluted in DCM, and then extracted four times with water. The combined organic phases were dried over sodium sulfate and purified by size exclusion chromatography to the final purified PF-127 conjugate with corresponding dye.

Sulfonated lissamine-alkyne PF-127 conjugate: 31 mg of a pink solid (yield: 57%), ^{1}H NMR (400 MHz, MeOD): δ = 8.65-6.70 (~11H, m, ar CH), 3.77-3.61 (-OCH$_2$CH$_2$O-) + 3.59-3.51 (m, -OCH$_2$CH-) + 3.43-3.38 (m, -CHCH$_3$) ~1000H, 1.04 (~195H, m, -CHCH$_3$). Degree of modification 61% (percentage of sulfonate lissamine-alkyne linked to pluronic).

5.3 Nanoparticle preparation. Stock solutions of the PLGA in acetonitrile were prepared at a concentration of 10 mg·mL^{-1} and, then, diluted with acetonitrile to 4 mg·mL^{-1}. The desired amount of R18/F5-TPB (typically 1 wt% relative to the polymer) or lumogen red (1wt%) was added. Under constant shaking, 50 µL of the polymer solution were quickly added using a micropipette (Thermomixer comfort, Eppendorf, 1100 rpm, 21°C) to 450 µL of milliQ water containing a chosen concentration of sodium chloride. Particle size was tuned by modulating sodium chloride concentration from 0 to 50 mM. The particle suspension was then quickly diluted 5-fold with water. For stabilization of NPs, different amounts of 1 or 0.1 mg mL^{-1} solutions of PF-127 or PF-68 were added under stirring to the NP solutions.

5.3.1 Instrumentation. The size and polydispersity index (PDI) measurements of the NPs were performed by DLS on a Zetasizer Nano series DTS 1060 (Malvern Instruments S.A.), using a 633 nm laser, which excludes any light excitation of our dye-loaded NPs. Absorption and emission spectra were recorded on a Cary 400 Scan ultraviolet-visible spectrophotometer (Varian) and a FluoroMax-4 spectro-fluorometer (Horiba Jobin Yvon) equipped with a thermostated cell compartment, respectively. For standard recording of fluorescence spectra, the excitation wavelength was set at 530 nm and emission was recorded from 540 to 800 nm. The fluorescence spectra were corrected for detector response and lamp fluctuations.

Fluorescence correlation spectroscopy (FCS) measurements were carried out on a two-photon platform based on Olympus IX70 inverted microscope. Two-photon excitation at 780 nm (5 mW laser output power) was provided using a mode-locked Tsunami Ti: sapphire laser pumped using a Millenia V solid state laser (Spectra Physics). The measurements were performed in an eight-well Lab-Tek II coverglass system, using 300 µL volume per well. The focal spot was set about 20 µm above the coverslip. The normalized autocorrelation function, $G(\tau)$, was calculated online using an ALV-5000E correlator (ALV, Germany) from the fluorescence fluctuations, $\delta F(t)$, by $G(\tau)= =<\delta F(t)\delta F(t+\tau)>/<F(t)>^2$ where t is the mean fluorescence signal and τ is the lag time. Assuming that NPs diffuse freely in a Gaussian excitation volume, the correlation function, $G(\tau)$, calculated from the fluorescence fluctuations was fitted according to Thompson [43]:

$$G(\tau)=\frac{1}{N}\left(1+\frac{\tau}{\tau_d}\right)^{-1}\left(1+\frac{1}{S^2}\frac{\tau}{\tau_d}\right)^{-1/2}$$

where τ_d is the diffusion time, N is the mean number of fluorescent species within the two-photon excitation volume, and S is the ratio between the axial and lateral radii of the excitation volume. The excitation volume is about 0.34 fL and S is about 3 to 4. The typical data recording time was 5 min. Measurements were done with respect to a reference 5(6)-carboxytetramethylrhodamine (TMR) (Sigma-Aldrich) in water.

5.3.2 Single-particle measurements on surfaces. NPs were immobilized on glass surface of LabTek slides as previously described [15]. Single-particle measurements were performed in the epi-fluorescence mode using Nikon Ti-E inverted microscope with CFI Plan Apo 60x oil (NA = 1.4) objective. The excitation was provided by light emitting diodes (SpectraX, Lumencor) at 550 nm at power density of 1.3 $W\cdot cm^{-2}$. The fluorescence signal was recorded with a Hamamatsu Orca Flash 4 camera. Integration time for a single frame was 200 ms. The single-particle analysis was performed using Fiji software, similarly to the previously described protocol [26]. Briefly, particle locations were detected through a FIJI routine applied to a

projection (maximum intensity) of 10 frames using an appropriate threshold. The mean intensities of circular regions of interest with a diameter of 6 pixels around the found particle locations were then measured. Background subtraction was then achieved by measuring the mean intensities in circular bands around the circular regions of interest and subtracting them. Finally, integrated intensity in all circular regions of interest (for the first 5 frames) was calculated and used for building the histograms of particle intensities.

5.4 Kinetics of NPs in the brain vasculature. All animal experiments were conducted in accordance with institutional guidelines and approved by the Government of Upper Bavaria. For real-time *in vivo* multiphoton imaging we used an upright Zeiss LSM710 microscope as described [28]. Briefly, 8-week old C56/Bl6N mice were anesthetized intraperitoneally with a combination of medetomidine (0.5 $mg \cdot kg^{-1}$), fentanyl (0.05 $mg \cdot kg^{-1}$), and midazolam (5mg kg^{-1}) (MMF). Then animals were endotracheally intubated and ventilated in a volume controlled mode (MiniVent 845, Hugo Sachs Elektronik, March-Hungstetten, Germany) with continuous recording of end-tidal pCO2. The body temperature was monitored throughout the experiment and maintained by a rectal probe attached to a feedback-controlled heating pad. The solutions containing PLGA NPs were injected through the intraartetiar femoral catheter, which was used also for measurement of mean arteriolar blood pressure. The intraviatl imaging was performed through a rectangular 4×4-mm glass cranial window at right fronto-parietal cortex, located 1-mm lateral to the sagittal suture and 1-mm frontal to the coronal suture made as described [28]. Afterwards, mice were placed on the multiphoton microscope adapted for intravital imaging of small animals. During imaging, first, mice were injected with FITC-dextran 3$\mu L \cdot g^{-1}$ to locate the region of interest (ROI). Upon identifying the ROI and scanning the baseline image, animals were administered with 7.5 $\mu L \cdot g^{-1}$ of PLGA NPs: bare (group of 3 animals) or F68 coated (group of 6 animals). The scanning was performed at 150 µm depth with laser power 4%-20%, laser frequency 800 nm and image acquisition was done through GAASP detector with LP<570 nm filter and master gain 600 for the FITC channel and LP>570 nm for the NPs channel with master gain 530.

5.4.1 Imaging analysis. The fluorescence analysis was performed using FIJI software. The Z-stack was converted to maximum intensity projection and the channels were split. The integrated density value of the each timepoint was divided (normalized) on the integrated density value of the baseline. To prevent fluctuation of the signal between animals, the signal from NPs channel was also divided (normalized) on FITC channel. The Two-way ANOVA statistical analysis with Tukey correction for multiple comparison was performed using Graph

Pad Prism 8.0.2. The video data as well as 3D-reconstraction was prepared using Imaris® software.

5.5 Evaluation of NPs bio-distribution *ex vivo*. C57Bl/6N male mice (23-25g) were injected intravenously (IV) with 7.5 µl·g^{-1} of PBS, PLGA-bare or P188-coated PLGA NPs solutions (*n*=3). 60 min post-injection, animals were anesthetized with a triple combination MMF (i.p.; 1 ml per 100 g body mass for mice). Upon the absence of the paw reflexes, the abdomen and chest were open and 25 G needle was inserted into the left ventricle for the perfusion with 0,9 % NaCl followed by 4 % PFA. The brain, liver, spleen, heart and kidney were extracted and fixed overnight in 4 % PFA.

5.5.1 Mouse tissue processing and staining.

5.5.1.1 Brains. The sectioning of brains into 50µm slices was done by Leica Vibratome, which were subsequently collected and kept in 0.1 m phosphate-buffered saline (PBS). The frontal, middle and caudal parts of each brain were taken for the staining. The free-floating sections were permeabilized in 24-well plates with 0.1% Tween20© (Carl Roth GmbH + Co. KG, Karlsruhe, Germany) in 0.1 m PBS and blocked with 10 % goat serum in 0.1 m PBS. Staining was performed with 1:1500 anti-Laminin (Rabbit, Sigma, #L9393) and anti-rabbit coupled to Alexa-fluor 647 (donkey anti-rabbit, Jackson Immuno Research, # 711-606-152, 1.5mg·mL^{-1} in 50% glycerol) as well as 1:200 anti-LAMP1 (rat, Santa Cruz, #sc-19992) and anti-rat coupled to Alexa-fluor 647 (donkey anti-rat, Jackson Immuno Research, #712-606-150, 1.5mg·mL^{-1} in 50% glycerol). Nuclei were stained with 4′,6-Diamidin-2-phenylindol (DAPI, Invitrogen, #D1306) 1:5000. DAPI, both primary and secondary antibodies were applied in 0.1 M PBS, because long-time exposure with triton or tween led to substantial leakage of NPs out of the tissue. Sections were mounted on microscope slides (Menzel-Gläser Superfrost® Plus, Thermo Fisher Scientific, #3502076) and covered with a coverslip (Menzel-Gläser 24–60 mm, #1, BB024060A1, Wagner und Munz) using aqueous mounting medium (CC/MountTM, Sigma-Aldrich, #C9368-30ML).

5.5.1.2 Internal organs. Free floating 50 µm sections of brain, liver, kidney, spleen and heart were prepared as previously described [28]. The sections were permeabilized for 30 minutes in PBS Tween 20, blocked for 60 minutes in 10% goat serum in PBS and then stained with the primary antibody for 12 hours at 4°C. The following primary antibodies were used: iba-1 (rabbit, Wako, #019-19741, 1:100), collagen IV (rabbit, Abcam, #ab19808, 1:100). After incubation sections were washed in PBS and incubated with the following secondary antibodies: anti-rabbit coupled to Alexa-fluor 594 (goat anti-rabbit, Thermo Fisher Scientific,

#A-11012). Nuclei were stained with 4',6-Diamidin-2-phenylindol (DAPI, Invitrogen, #D1306) 1:10,000 in 0.01 M PBS.

5.5.2 Ex vivo imaging and analysis.

5.5.2.1 Brains. The whole hemisphere images were acquired using a Zeiss confocal microscope with 40x magnification (objective: EC Plan-Neofluar 40x/1.30 Oil DIC M27) with an image matrix of 512×512 pixel, a pixel scaling of 0.593×0.593 µm and a depth of 8 bit. Confocal-images were collected in tile scan Z-stacks 10 slices with a slice-distance of 2 µm. Single particles images were acquired with 100x magnification (alpha Plan-Apochromat 100x/1.46 Oil DIC M27 Elyra) with an image matrix 2048×2048, a pixel scaling of 0.059 µm x×0.059 µm and a depth of 8 bit. Morphological analysis was performed using FIJI software. The whole brain hemisphere was selected as a region of interest and the channels were split. The mean grey value of the rhodamine channel was divided (normalized) on the mean grey value of the DAPI channel. The One-way ANOVA statistical analysis with Tukey correction for multiple comparison was performed using Graph Pad Prism 8.0.2. Analysis of single particles in the brain parenchyma was performed using green 488 channel as a reference for the auto-fluorescence. Only red dotty structures that were strongly not co-localized with the green 488 channel had been considered as NPs. On merged image, the co-localized dots had yellowish colour, while NPs were red. The quantification of the autofluorescent particles (n=3, ROI=5): the number of co-localized (yellow colour) foci in the ROI was divided on the ROI's area and cell numbers. The quantification of the single particles (n=3, ROI=5): the number of non-co-localized (red colour) foci in the ROI was normalized to the ROI area and cell numbers. The unpaired t-test was used for statistical analysis using Graph Pad Prism 8.0.2. The video data as well as 3D-reconstraction was prepared using Imaris® software.

5.5.2.2 Internal organs. Imaging was performed using confocal microscopy (ZEISS LSM 900, Carl Zeiss Microscopy GmbH, Jena Germany). For general biodistribution in organs, pictures were collected as 3 x 3 tile scans at 25x magnification (objective: i LCI Plan-Neofluar 25x/0.8 Imm Korr DIC M27) with an image matrix of 512x512, a pixel scaling of 1.107x0.107 µm and a depth of 8 bit. Three different brain sections per animal were chosen and collected in 15,9 µm z-stacks with a slice distance of 2,65 µm. For colocalization analysis, 40x magnification (objective: EC Plan-Neofluar 40x/1.30 Oil DIC M27) was used with an image matrix of 512×512, a pixel scaling of 0.415×0.415 µm and a depth of 16 bit. Three to four ROIs per animal were collected in z-stacks as tile scans with a slice-distance of 1.07 µm and a total range of 5.35 µm.

Quantification of biodistribution of NPs in the internal organs was performed using ImageJ [44] in unstained sections of brain, liver, kidney, spleen and heart. Maximum intensity projection of the Z -stacks were imported into the software and split into individual channels. Intensity of NPs (rhodamine channel) was then measured using the mean grey value per area and normalized to intensity of auto-fluorescent signal (green channel).

For the co-localization analysis, we exploited, ImageJ compatible, JACoP Plugin [45]. Z-stacks were imported into the software in split into individual channels. The rhodamine channel for nanoparticles and the far red channel for either iba-1 or collagen IV were selected for co-localization analysis and thresholds were set using Costes' automatic threshold as described previously [46]. Finally, the plugin calculates colocalization using the Manders' overlap coefficient, established by Manders *et al.* [33]. This coefficient represents the ratio of summed intensities of particles in the predefined green and red channels and therefore indicates the proportion of NPs overlapping with iba-1 or collagen IV over their whole intensity. The Manders coefficient varies between 0 and 1, with 0 meaning no overlap and 1 being perfect colocalization. This can be done throughout the Z-stack without having to take the maximum intensity projection, therefore reducing signal loss through overlay of NPs.

Supporting information

Supporting Information containing figures and movies are available at website.

Acknowledgements

This project was funded by the Alexander von Humboldt Foundation, the European Union Horizon 2020 research and innovation program under the Marie Skłodowska-Curie grant agreement No 794094, the European Research Council ERC Consolidator grant BrightSens 648528, the Agence National de Recherche JC/JC grant "Supertrack" ANR-16-CE09-0007, the DFG under the Munich Cluster of Systems Neurology (Synergy), and ERA-NET Neuron TRAINS.

Conflict of interest

Authors declare no financial or commercial Conflict of Interest.

References:

1. Cai, Q., et al., *Systemic delivery to central nervous system by engineered PLGA nanoparticles.* American journal of translational research, 2016. **8**(2): p. 749-764.
2. Kumari, A., S.K. Yadav, and S.C. Yadav, *Biodegradable polymeric nanoparticles based drug delivery systems.* Colloids Surf B Biointerfaces, 2010. **75**(1): p. 1-18.
3. Blasi, P., *Poly(lactic acid)/poly(lactic-co-glycolic acid)-based microparticles: an overview.* Journal of Pharmaceutical Investigation, 2019. **49**(4): p. 337-346.

4. Wang Y, Q.W., Choi SH, *FDA's regulatory science program for generic PLA/PLGA-based drug products.* American Pharmaceutical Review, 2017. **19**(4): p. 5-9.
5. Alyautdin, R., et al., *Nanoscale drug delivery systems and the blood-brain barrier.* International journal of nanomedicine, 2014. **9**: p. 795-811.
6. Jones, A.A.D., III, G. Mi, and T.J. Webster, *A Status Report on FDA Approval of Medical Devices Containing Nanostructured Materials.* Trends in Biotechnology, 2019. **37**(2): p. 117-120.
7. Khalin, I., et al., *Brain-derived neurotrophic factor delivered to the brain using poly (lactide-co-glycolide) nanoparticles improves neurological and cognitive outcome in mice with traumatic brain injury.* Drug Deliv, 2016. **23**(9): p. 3520-3528.
8. Gelperina, S., et al., *Drug delivery to the brain using surfactant-coated poly(lactide-co-glycolide) nanoparticles: Influence of the formulation parameters.* European Journal of Pharmaceutics and Biopharmaceutics, 2010. **74**(2): p. 157-163.
9. Hartl, N., F. Adams, and O.M. Merkel, *From Adsorption to Covalent Bonding: Apolipoprotein E Functionalization of Polymeric Nanoparticles for Drug Delivery Across the Blood–Brain Barrier.* Advanced Therapeutics, 2020: p. 2000092.
10. Saraiva, C., et al., *Nanoparticle-mediated brain drug delivery: Overcoming blood–brain barrier to treat neurodegenerative diseases.* Journal of Controlled Release, 2016. **235**: p. 34-47.
11. Kreuter, J., *Drug delivery to the central nervous system by polymeric nanoparticles: what do we know?* Adv Drug Deliv Rev, 2014. **71**: p. 2-14.
12. Wu, C. and D.T. Chiu, *Highly Fluorescent Semiconducting Polymer Dots for Biology and Medicine.* Angewandte Chemie International Edition, 2013. **52**(11): p. 3086-3109.
13. Li, K. and B. Liu, *Polymer-encapsulated organic nanoparticles for fluorescence and photoacoustic imaging.* Chemical Society Reviews, 2014. **43**(18): p. 6570-6597.
14. Mei, J., et al., *Aggregation-Induced Emission: Together We Shine, United We Soar!* Chemical Reviews, 2015. **115**(21): p. 11718-11940.
15. Reisch, A., et al., *Collective fluorescence switching of counterion-assembled dyes in polymer nanoparticles.* Nat Commun, 2014. **5**: p. 4089.
16. Runser, A., et al., *Zwitterionic Stealth Dye-Loaded Polymer Nanoparticles for Intracellular Imaging.* ACS Applied Materials & Interfaces, 2020. **12**(1): p. 117-125.
17. Reisch, A., et al., *Protein-Sized Dye-Loaded Polymer Nanoparticles for Free Particle Diffusion in Cytosol.* Advanced Functional Materials, 2018. **28**(48): p. 1805157.
18. Cardoso Dos Santos, M., et al., *Lanthanide-Complex-Loaded Polymer Nanoparticles for Background-Free Single-Particle and Live-Cell Imaging.* Chemistry of Materials, 2019. **31**(11): p. 4034-4041.
19. Melnychuk, N., et al., *Light-Harvesting Nanoparticle Probes for FRET-Based Detection of Oligonucleotides with Single-Molecule Sensitivity.* Angewandte Chemie International Edition, 2020. **59**(17): p. 6811-6818.
20. Melnychuk, N. and A.S. Klymchenko, *DNA-Functionalized Dye-Loaded Polymeric Nanoparticles: Ultrabright FRET Platform for Amplified Detection of Nucleic Acids.* Journal of the American Chemical Society, 2018. **140**(34): p. 10856-10865.
21. Trofymchuk, K., et al., *Giant light-harvesting nanoantenna for single-molecule detection in ambient light.* Nature Photonics, 2017. **11**(10): p. 657-663.
22. Reisch, A., et al., *Tailoring Fluorescence Brightness and Switching of Nanoparticles through Dye Organization in the Polymer Matrix.* ACS Appl Mater Interfaces, 2017. **9**(49): p. 43030-43042.
23. Lepeltier, E., C. Bourgaux, and P. Couvreur, *Nanoprecipitation and the "Ouzo effect": Application to drug delivery devices.* Advanced Drug Delivery Reviews, 2014. **71**: p. 86-97.

24. Saad, W.S. and R.K. Prud'homme, *Principles of nanoparticle formation by flash nanoprecipitation.* Nano Today, 2016. **11**(2): p. 212-227.
25. Trofymchuk, K., et al., *Tuning the color and photostability of perylene diimides inside polymer nanoparticles: towards biodegradable substitutes of quantum dots.* Nanoscale, 2014. **6**(21): p. 12934-12942.
26. Reisch, A., et al., *Charge-Controlled Nanoprecipitation as a Modular Approach to Ultrasmall Polymer Nanocarriers: Making Bright and Stable Nanoparticles.* ACS Nano, 2015. **9**(5): p. 5104-5116.
27. Egloff, S., et al., *Size-Dependent Electroporation of Dye-Loaded Polymer Nanoparticles for Efficient and Safe Intracellular Delivery.* 2021. **5**(2): p. 2000947.
28. Khalin, I., et al., *Ultrabright Fluorescent Polymeric Nanoparticles with a Stealth Pluronic Shell for Live Tracking in the Mouse Brain.* ACS nano, 2020. **14**(8): p. 9755-9770.
29. Gref, R., et al., *'Stealth' corona-core nanoparticles surface modified by polyethylene glycol (PEG): influences of the corona (PEG chain length and surface density) and of the core composition on phagocytic uptake and plasma protein adsorption.* Colloids and Surfaces B: Biointerfaces, 2000. **18**(3): p. 301-313.
30. Würth, C., et al., *Comparison of Methods and Achievable Uncertainties for the Relative and Absolute Measurement of Photoluminescence Quantum Yields.* Analytical Chemistry, 2011. **83**(9): p. 3431-3439.
31. De Belder, G., et al., *Singlet–Singlet Annihilation in Multichromophoric Peryleneimide Dendrimers, Determined by Fluorescence Upconversion.* 2001. **2**(1): p. 49-55.
32. Pöschl, E., et al., *Collagen IV is essential for basement membrane stability but dispensable for initiation of its assembly during early development.* Development, 2004. **131**(7): p. 1619-1628.
33. Manders, E.M., et al., *Dynamics of three-dimensional replication patterns during the S-phase, analysed by double labelling of DNA and confocal microscopy.* J Cell Sci, 1992. **103 (Pt 3)**: p. 857-62.
34. Donovan, K.M., et al., *Allograft Inflammatory Factor 1 as an Immunohistochemical Marker for Macrophages in Multiple Tissues and Laboratory Animal Species.* Comparative medicine, 2018. **68**(5): p. 341-348.
35. Munter, R., et al., *Dissociation of fluorescently labeled lipids from liposomes in biological environments challenges the interpretation of uptake studies.* Nanoscale, 2018. **10**(48): p. 22720-22724.
36. Andreiuk, B., et al., *Fighting Aggregation-Caused Quenching and Leakage of Dyes in Fluorescent Polymer Nanoparticles: Universal Role of Counterion.* 2019. **14**(6): p. 836-846.
37. Monici, M., *Cell and tissue autofluorescence research and diagnostic applications.* 2005. **11**: p. 227-256.
38. Blanco, S., et al., *Hyaluronate Nanoparticles as a Delivery System to Carry Neuroglobin to the Brain after Stroke.* 2020. **12**(1): p. 40.
39. Engel, D.C., et al., *Changes of cerebral blood flow during the secondary expansion of a cortical contusion assessed by 14C-iodoantipyrine autoradiography in mice using a non-invasive protocol.* J Neurotrauma, 2008. **25**(7): p. 739-53.
40. Moghimi, S.M., *Prolonging the circulation time and modifying the body distribution of intravenously injected polystyrene nanospheres by prior intravenous administration of poloxamine-908. A 'hepatic-blockade' event or manipulation of nanosphere surface in vivo?* Biochimica et biophysica acta, 1997. **1336**(1): p. 1-6.
41. Andreiuk, B., et al., *Fluorescent Polymer Nanoparticles for Cell Barcoding In Vitro and In Vivo.* Small, 2017. **13**(38): p. 1701582.

42. Hatai, J., L. Motiei, and D. Margulies, *Analyzing Amyloid Beta Aggregates with a Combinatorial Fluorescent Molecular Sensor.* Journal of the American Chemical Society, 2017. **139**(6): p. 2136-2139.
43. *Topics in Fluorescence Spectroscopy: Principles*. Topics in Fluorescence Spectroscopy 2002: Springer US. XVI, 432.
44. Schindelin, J., et al., *Fiji: an open-source platform for biological-image analysis.* Nat Methods, 2012. **9**(7): p. 676-82.
45. Bolte, S. and F.P. Cordelieres, *A guided tour into subcellular colocalization analysis in light microscopy.* J Microsc, 2006. **224**(Pt 3): p. 213-32.
46. Costes, S.V., et al., *Automatic and quantitative measurement of protein-protein colocalization in live cells.* Biophys J, 2004. **86**(6): p. 3993-4003.

Supporting information

Cerebral biodistribution and real-time particle tracking *in vivo* of ultrabright fluorescent PLGA nano-carriers

Igor Khalin,[1,3*] *Caterina Severi,*[2] *Doriane Heimburger,*[2] *Antonia Wehn*[1,3], *Farida Hellal*[1,3,4], *Andreas Reisch,*[2*] *Andrey S. Klymchenko*[2*], *Nikolaus Plesnila*[1,3*]

1. Institute for Stroke and Dementia Research (ISD), Klinikum der Universität München, Feodor-Lynen-Straße 17, D-81377 Munich, Germany

2. Laboratoire de Bioimagerie et Pathologies, UMR 7021 CNRS, Université de Strasbourg, Faculté de Pharmacie, 74, Route du Rhin, 67401 Illkirch, France

3. Cluster for Systems Neurology (SyNergy), Munich, Germany

4. Institute of Tissue Engineering and Regenerative Medicine (iTERM), Helmholz Zentrum Muenchen, Ingolstaedter Landstrasse 1, 85764 Neuherberg, Germany

*Corresponding authors: igor.khalin@med.uni-muenchen.de; reisch@unistra.fr; andrey.klymchenko@unistra.fr; nikolaus.plesnila@med.uni-muenchen.de

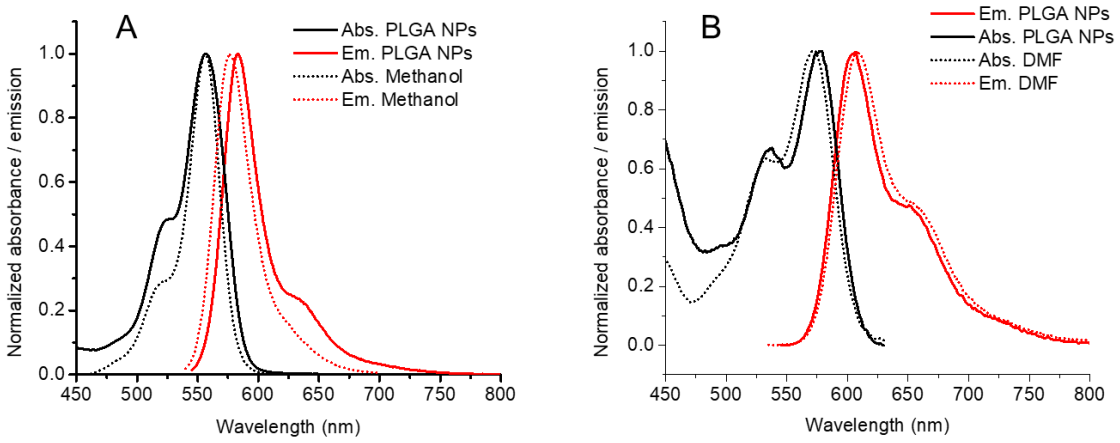

Figure S1. Normalized absorption (black) and emission (red) spectra of R18/F5-TPB (A) and Lumogen Red (B) in PLGA NPs (solid lines) and in an organic solvent (dotted lines).

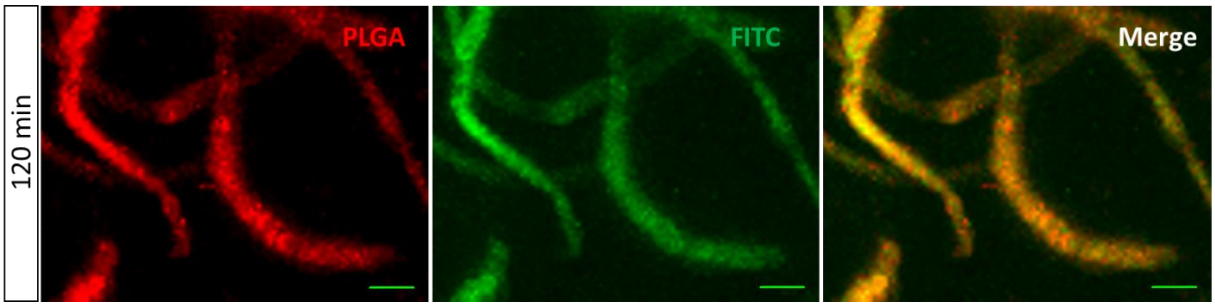

Figure S2. Accumulation of PLGA NPs in the vessels's wall 120 minutes post-injection. Scanned images 120 minutes after injection of FITC-dextran 2000kDa and coated PLGA-F68 NPs. Z-stack, maximum intensity projection. Scale bar - 10 μm.

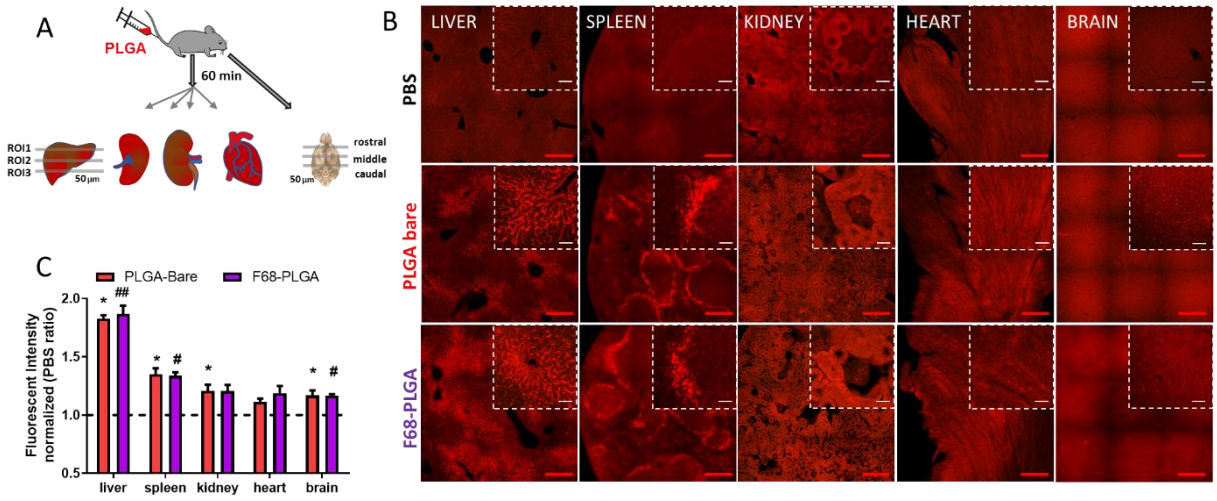

Figure S3. Biodistribution of PLGA-coated and -uncoated NPs in the mouse liver, spleen, kidney, heart and brain 60 minutes post-injection. **A:** Experimental design. **B**: Representative 25x confocal images of unstained sections of all organs from animals injected with PBS, bare or coated NPs. Maximum intensity projection of rhodamine channel of tile scans and zoomed single tile indicated by dashed line. Scale bar – 200 µm (red), 50 µm (white). **C:** Quantification of distribution of the NPs throughout all organs analysed using FIJI: the mean grey value of the rhodamine channel normalized to the mean grey value of the green autofluorescent channel adjusted for ROI area (μm^2). Data presented as means ± standard deviation (SD). For the statistical analysis, Kruskal-Wallis One Way Analysis of Variance on Ranks was used followed by Dunn's multiple comparison. * $p<0.05$ bare compared to PBS group; # $p<0.05$ coated compared to PBS group; ## $p<0.005$ coated compared to PBS group; n=2-3 animals x 3 sections per organ (rostral, middle, caudal).

Supporting movies

Movie S1. Bare PLGA particles circulating in the mouse brain vasculature. Scanned images 5 min after injection of NPs solution. Rendered Z-stack, 150 μm depth. Laser power 3.5%-10%. Green - FITC-dextran (2000kDa), red foci – bare PLGA NPs, 70 nm. Scale bar - 50 μm.

Movie S2. PF-68 costed PLGA particles circulating in the mouse brain vasculature. Scanned images 5 min after injection of NPs solution. Rendered Z-stack, 150 μm depth. Laser power 3.5%-10%. Green - FITC-dextran (2000kDa), red – coated PLGA NPs, 70 nm. Scale bar - 50 μm.

Movie S3. 3D reconstruction of brain capillary with accumulated PF-68 coated PLGA NPs. Rhodamine channel shows non-specific red foci. Auto-fluorescent channel shows auto-fluorescent foci of the brain parenchyma. Red arrow indicates the PLGA NPs, while white arrow - auto-fluorescence as a co-localization between rhodamine and auto-fluorescent channels. Laminin stains basal membrane, which outlines the spatial distribution of NPs.

Movie S4. 3D reconstruction of LAMP1 positive cell compartments; red – NPs; green – autofluorescence; white and red – a co-localization of NPs and LAMP1; white and green – a co-localization of autofluorescent focus and LAMP1.

Movie S5. 3D reconstruction of PLGA NPs uptaken by Kuppfer cell (Iba-1 positive) of the mouse injected by bare NPs.

Movie S6. 3D reconstruction of PLGA NPs uptaken by Kuppfer cell (Iba-1 positive) of the mouse injected by PF-68 coated NPs.